LANGMUIR Article
Cite This: Langmuir 2019, 35, 12158−12167
pubs.acs.org/Langmuir

# Experiments and Simulations on the Magnetorheology of Magnetic Fluid Based on $Fe_3O_4$ Hollow Chains

Lei Pei,[†] Shouhu Xuan,*[,†] Jie Wu,[†] Linfeng Bai,[‡] and Xinglong Gong*[,†]

[†]CAS Key Laboratory of Mechanical Behavior and Design of Materials, CAS Center for Excellence in Complex System Mechanics, Department of Modern Mechanics and [‡]Department of Chemistry, University of Science and Technology of China, Hefei, Anhui, 230027, China

Supporting Information

**ABSTRACT:** This work reports an experiment/simulation combination study on the magnetorheological (MR) mechanism of magnetic fluid based on $Fe_3O_4$ hollow chains. The decrease of shear stress versus the increasing magnetic field was observed in a dilute magnetic fluid. Hollow chains exhibited a higher MR effect than pure $Fe_3O_4$ hollow nanospheres under a small magnetic field. A modified particle level simulation method including the translational and rotational motion of chains was developed to comprehend the correlation between rheological properties and microstructures. Sloping cluster-like microstructures were formed under a weak external field (24 mT), while vertical column-like microstructures were observed under a strong field (240 mT). The decrease of shear stress was due to the strong reconstruction process of microstructures and the agglomeration of chains near the boundaries. The chain morphology increased the dip angle of microstructures and thus improved the MR effect under a weak field. This advantage made $Fe_3O_4$ hollow chains to be widely applied for small and low-power devices in the biomedical field. Dimensionless viscosity as a function of the Mason number was collapsed onto linear master curves. Magnetic fluid in Poiseuille flow in a microfluidic channel was also observed and simulated. A qualitative and quantitative correspondence between simulations and experiments was obtained.

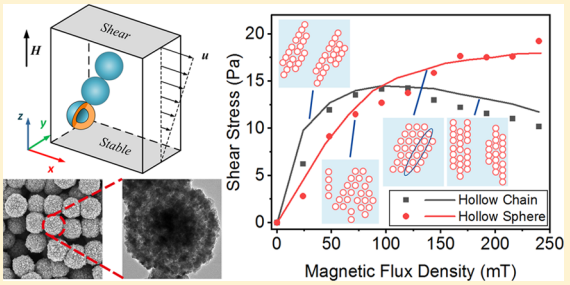


## INTRODUCTION

The magnetic fluid is a suspension of micro- or nanoscale magnetizable particles in a nonmagnetic carrier fluid.[1] Based on the diameter and magnetic properties of particles, magnetorheological (MR) fluid and ferrofluid can be distinguished.[2] When exposed to an external magnetic field, particles will interact with each other and rearrange into chain-like microstructures. The yield stress and viscosity of magnetic fluid will increase by several orders of magnitude within a few milliseconds.[3,4] The reversible MR effect makes magnetic fluids be widely utilized in polishing, brakes, dampers, and energy absorbers.[4−8] Among the conventional magnetic materials, magnetite ($Fe_3O_4$) possesses numerous unique properties such as a wide range of diameter, good biocompatibility, and easy to modify the surface. Magnetic fluid based on $Fe_3O_4$ opens a promising avenue in magnetic thermal therapy and drug targeting delivery.[9−11] In the biomedical field, the size and energy consumption of devices are supposed to be as small as possible. Magnetic fluid should exhibit an excellent MR effect under a small field. This performance is related to the magnetization, morphology, and inner architecture of magnetic particles. It is reported that magnetic fluid based on rod-like or fibrous particles exhibited a superior MR effect.[12−14] However, these novel particles cannot overcome the sediment problem due to the inherent density mismatch with the carrier fluid.

Hollow nanospheres are promising architectures to improve the MR effect and reduce the particle density at the same time.[15−18] Cheng et al. synthesized hollow $Fe_3O_4$ nanospheres via a one-pot hydrothermal method.[19] The prepared hollow spheres presented excellent redispersibility, indicating good antisedimentation stability. Rheological properties of hollow $Fe_3O_4$ spheres with different diameters were also studied.[20] The yield stress of submicron hollow spheres reached 4.39 times larger than that of small solid ones. Hollow $Fe_3O_4$ also possessed lower density, higher saturation magnetization, and lower sedimentation rate. By combining the chain morphology and hollow inner architecture together, the shear stress of magnetic fluid based on $Fe_3O_4$ hollow chains could be strengthened compared to hollow spheres. This novel hollow chain displays a wide prospect of applications in small and low-power devices. The rheological properties of magnetic fluid are governed by the evolution of microstructures. Its unique rheological behaviors originate from special microstructures as a result of the particular morphology and interparticle forces. To better comprehend the correlation between macroscopic properties and microstructures has become an urgent require-

Received: June 26, 2019
Revised: August 21, 2019
Published: August 26, 2019






DOI: 10.1021/acs.langmuir.9b01957
Langmuir 2019, 35, 12158−12167

ment for both fundamental interest and applications. However, the particle level MR mechanism has not been investigated yet.

In recent years, simulation has become a useful tool in mechanism research of magnetic fluid due to the improvement of computer performance. Several powerful simulation methods have been developed such as molecular dynamics, particle level dynamic simulation, finite element method, computational fluid dynamics, and machine learning method.[21−25] Particle level dynamic simulation is a mesoscopic simulation method based on the point-dipole model.[26] This numerical method has been employed to investigate conventional magnetic fluid under different loadings. Ruiz-López et al. systematically discussed the rheological behavior of ferrofluid under steady and oscillatory shear by combining theories, experiments, and particle level simulations together.[27] The influence of particle volume fractions was explained by the variation of microstructures. Rearrangement of particles in the squeeze flow mode was also studied using particle level dynamic simulations.[28] Simulated yield stress matched well with rheological tests. In particular, this simulation method has been introduced to the hollow sphere system.[29] The superior MR effect of the hollow architecture was interpreted by the unique microstructures. The optimal diameter and wall thickness of hollow $Fe_3O_4$ nanospheres were determined through the simulation.[30] With the development of theories on rod-like magnetic particles, particle level dynamic simulation became a powerful approach to investigate this novel hollow chain system.[31−33]

In this work, a combination of experiments and simulations was used to study the MR mechanism of magnetic fluid based on $Fe_3O_4$ hollow chains. First, $Fe_3O_4$ chains composed of hollow nanospheres were synthesized and characterized. Rheological tests showed hollow chains presented a superior MR effect to hollow spheres under a small magnetic field. A modified particle level simulation model considering the translational and rotational motion of chains was then used. The correlation between rheological properties and microstructures of magnetic fluid was systematically discussed. A mesoscopic mechanism was developed to comprehend the advantages of $Fe_3O_4$ hollow chains. Viscosity was collapsed onto several master curves using the dimensionless Mason number. Finally, a good correspondence between simulations and experiments was obtained.

## EXPERIMENTAL SECTION

**Chemicals.** Ferric chloride hexahydrate ($FeCl_3{\cdot}6H_2O$), urea ($CO(NH_2)_2$), sodium citrate ($C_6H_5Na_3O_7{\cdot}2H_2O$), polyacrylamide-3000000 (PAM), and polyvinylpyrrolidone (PVP) were purchased from Sinopharm Chemical Reagent Co, Ltd. All the reagents were of analytical grade and used without further purification. Deionized water was used for the synthesis of $Fe_3O_4$ hollow chains.

**Synthesis of $Fe_3O_4$ Hollow Chains.** $Fe_3O_4$ chains based on hollow nanospheres were synthesized via a hydrothermal method. First, 1 mmol of $FeCl_3{\cdot}6H_2O$, 2 mmol of $C_6H_5Na_3O_7{\cdot}2H_2O$, and 3 mmol of $CO(NH_2)_2$ were dissolved in 40 mL of deionized water. After vigorous stirring, 0.15 g of PAM and 0.1 g of PVP were added into the solution. The solution was kept under stirring at 300 rpm for 1 h, and then the mixture was transferred into a 25 mL Teflon-lined autoclave. A small magnet was placed at the bottom, and the autoclave was sealed to heat at 200 °C for 12 h. After the reaction, the autoclave was naturally cooled to room temperature. The products were washed with water and ethanol for four times and then dried in a vacuum oven to get a black powder. Finally, the $Fe_3O_4$ hollow chains were dispersed into water with weight fractions of 10, 15, and 20 wt % to form magnetic fluids.

**Characterization.** Transmission electron microscopy (TEM) images were observed using a high-resolution TEM (JEM-2100F, JEOL Co., Japan) with an accelerating voltage of 200 kV. The scanning electron microscopy (SEM) photographs were taken on a field emission scanning electron microscope (JSM-6700F, JEOL Co., Japan). The magnetic hysteresis loop at room temperature was characterized using a hysteresiscope (SQUID VSM, Quantum Design Co., America) with an applied field from −30 to 30 kOe. In order to verify the simulated microstructures, snapshots of magnetic fluid in a microfluidic channel were taken using an optical microscope (ICX40, Sunny Optical Technology Co., China) and a high-speed camera (Phantom V2512, Phantom Co., America).

The rheological properties of magnetic fluids were measured by a commercial rheometer (Physica MCR 301, Anton Paar Co., Austria). Typically, the magnetic fluid was placed between two parallel plates (PP20/MRD) with a gap of 0.8 mm. The shear loading was applied through the rotating upper plate. A built-in electromagnet and a permeable framework generated a uniform magnetic field perpendicular to the shear flow. Magnetic field sweep tests were conducted at a shear rate of 100 $s^{-1}$ with an external field from 0 to 240 mT. The flow curves were obtained under applied fields of 0, 48, 96, and 240 mT with logarithmically increasing shear rates from 0.01 to 100 $s^{-1}$. A pre-shear of 30 s was carried out to remove the history-dependent microstructures. The temperature was maintained at 25 °C during all the tests.

## SIMULATION MODEL

**Simulation Conditions.** A cubic simulation box and a Cartesian coordinate system are employed in the simulation. Periodic boundary conditions on the $x-z$ and $y-z$ planes are imposed, while shear boundary conditions are applied on the $x-y$ plane. The matrix is supposed to fill the hollow chains and unable to flow into or out of the chains during the simulation. The lengths of $Fe_3O_4$ hollow chains are set between $N = 3$ and 9 with an average value of $N = 6$ according to experiments. The number of chains is maintained at 300. For simplicity, $Fe_3O_4$ hollow chains are randomly distributed in the simulation box with a fixed orientation along the $z$ axis at the initial state. Strictly speaking, $Fe_3O_4$ hollow chains should align along the shear direction ($x$ axis) after the pre-shear process. The reason to choose such initial conditions is discussed in Figure S1. At the same time, an external magnetic field along the $z$ axis and a steady shear flow along the $x$ axis are suddenly applied. The system starts to evolve until the shear stress reaches homeostasis.

**Interactions among Chains.** It is assumed that each $Fe_3O_4$ hollow chain is a rigid array of monodisperse hollow nanospheres. According to the superposition principle, the magnetic fluid is modeled as a system of hollow nanospheres when calculating the magnetization and forces among $Fe_3O_4$ chains. The correlation between magnetization $M$ and external field strength $H$ of super-paramagnetic $Fe_3O_4$ nanospheres can be characterized by the Langevin function[34]

$$M = M_s\left[\coth\left(\frac{H}{x}\right) - \frac{x}{H}\right] \tag{1}$$

where $x$ is a constant related to the material and size of nanospheres and $M_s$ means the saturation magnetization. $Fe_3O_4$ hollow spheres and solid spheres exhibited the same magnetic hysteresis loop.[29] Equation 1 is also applicable for the hollow sphere system. Thus, the magnetic moment induced by the external field can be determined as

$$\boldsymbol{m}_i = MV_p\frac{\boldsymbol{H}}{H} \tag{2}$$



DOI: 10.1021/acs.langmuir.9b01957
Langmuir 2019, 35, 12158−12167

where $V_p$ represents the volume of the solid part of hollow nanospheres and $H = |\mathbf{H}|$. After being magnetized by the external field, sphere $i$ will generate a magnetic field at the position of sphere $j$

$$\boldsymbol{H}_i = -\frac{1}{4\pi {r_{ij}}^3}[\boldsymbol{m}_i - 3(\boldsymbol{m}_i \cdot \hat{\boldsymbol{r}})\hat{\boldsymbol{r}}] \tag{3}$$

where $r_{ij}$ indicates the distance between these two spheres and $\hat{\mathbf{r}}$ is a unit vector from $i$ to $j$. The total magnetic moment of a single nanosphere is obtained using the superposition method:

$$\boldsymbol{m}_i = M_s\left[\coth\left(\frac{H_{loc}}{x}\right) + \frac{x}{H_{loc}}\right]V_p\frac{\boldsymbol{H}_{loc}}{H_{loc}},\ \boldsymbol{H}_{loc} = \boldsymbol{H} + \sum_{j\neq i}\boldsymbol{H}_j \tag{4}$$

The last term in eq 4 represents the direction of the moment vector.

According to the point-dipole model, the magnetic force imposed on sphere $i$ exerted by sphere $j$ is given by

$$\boldsymbol{F}_{ij}^m = \frac{3\mu_0}{4\pi {r_{ij}}^4}c_m[(-\boldsymbol{m}_i\cdot\boldsymbol{m}_j + 5\boldsymbol{m}_i\cdot\hat{\boldsymbol{r}}\ \boldsymbol{m}_j\cdot\hat{\boldsymbol{r}})\hat{\boldsymbol{r}} - (\boldsymbol{m}_i\cdot\hat{\boldsymbol{r}})\boldsymbol{m}_j - (\boldsymbol{m}_j\cdot\hat{\boldsymbol{r}})\boldsymbol{m}_i] \tag{5}$$

Here, the magnetic permeability of the matrix is approximately equal to $\mu_0 = 4\pi \times 10^{-7}$ N/A$^2$. $c_m$ is a factor to correct the dipole model when two spheres are very close to each other.[35] Each chain will also experience a magnetic torque due to the external field

$$\boldsymbol{T}^m = \mu_0\sum_{i=1}^{N}\boldsymbol{m}_i \times \boldsymbol{H} \tag{6}$$

where $N$ is the number of nanospheres in the chain.

The van der Waals force between two nanospheres is expressed as[30]

$$\boldsymbol{F}_{ij}^{vdw} = \frac{8A}{3}L_{ij}d_id_j\left[\frac{1}{4{L_{ij}}^2 - (d_i + d_j)^2} - \frac{1}{4{L_{ij}}^2 - (d_i - d_j)^2}\right]^2\hat{\boldsymbol{r}} \tag{7}$$

The Hamaker constant of $Fe_3O_4$ is $A = 3 \times 10^{-20}$ J.[36] $L_{ij} = \max[r_{ij}, d_{ij} + h_{min}]$, $h_{min} = 0.01d_{ij}$, and $d_{ij} = (d_i + d_j)/2$.[37] $d_i$ and $d_j$ are the diameters of nanospheres. In this work, each hollow sphere is considered as a big solid sphere and an overlapped small solid sphere with a negative mass and magnetization. Both magnetic force and van der Waals force between two hollow nanospheres include a big−big interaction, a small−small interaction, and a pair of big−small interaction. The correction factor $c_m$ is separately employed in the three parts of magnetic force.

In order to avoid the overlap of nanospheres, an exponential repulsive force is introduced[38]

$$\boldsymbol{F}_{ij}^r = -\left(\frac{3\mu_0 {M_s}^2 {V_p}^2}{2\pi d^4} + \boldsymbol{F}_{ij}^{vdw}\right)10^{-10\left(\frac{r_{ij}}{d}-1\right)}\hat{\boldsymbol{r}} \tag{8}$$

where $d$ is the average diameter of hollow nanospheres.

**Relative Motion of Chains in the Matrix.** In a magnetic fluid, the motion of $Fe_3O_4$ hollow chains relative to the matrix belongs to Stokes flow with a Reynolds number of $Re = 0$. The drag force of a $Fe_3O_4$ hollow chain is in proportion to the relative velocity

$$\boldsymbol{F}^d = -3\pi\eta d\xi_N\boldsymbol{u}_c \tag{9}$$

where $\xi_N$ is a function of the length and orientation of the chain and $\mathbf{u}_c$ is the relative velocity of the center of the chain. Analytical drag coefficients of a two-bead chain have been proposed by Swanson et al.[39] Yang et al. and Yamakawa and Tanaka further investigated translational drag coefficients of magnetic bead-chains with different lengths.[40,41] Experimental observations revealed that $Fe_3O_4$ hollow chains almost aligned along the direction of the external field, which is perpendicular to the flow direction. Therefore, $\xi_N$ is chosen as the perpendicular drag coefficients in the literature[41]

$$\xi_N = \frac{4}{3}\frac{N}{\ln(N) + 1.111} \tag{10}$$

If a rigid bead-chain is rotating in a stationary Newtonian fluid, the viscous drag torque can be written as[42]

$$\boldsymbol{T}^d = \frac{1}{3}\pi d^3\frac{N^3}{\ln(N/2)}\eta\boldsymbol{\omega} \tag{11}$$

where $\boldsymbol{\omega}$ represents the angular speed of the chain. After applying plane shear flow, the expression of $\mathbf{T}^d$ will become very complex. Sánchez and Rinaldi extensively discussed the hydrodynamic torque on an ellipsoidal rigid body in shear flow.[43] For simplicity, each nanosphere is assumed to experience a drag force

$$\boldsymbol{F}_i^d = -3\pi\eta d\frac{\xi_N}{N}\boldsymbol{u}_i \tag{12}$$

where $\mathbf{u}_i = \mathbf{u}_c + (\boldsymbol{\omega} - \boldsymbol{\omega}_f) \times (\mathbf{r}_i - \mathbf{r}_c)$ is the relative velocity of sphere $i$. $\mathbf{r}_i$ and $\mathbf{r}_c$ are the position vectors of sphere $i$ and the center of the chain. $\boldsymbol{\omega}_f$ is the angular speed of the matrix. Hence, the hydrodynamic torque on a chain is given as

$$\boldsymbol{T}^d = \sum_{i=1}^{N}(\boldsymbol{r}_i - \boldsymbol{r}_c) \times \boldsymbol{F}_i^d \tag{13}$$

The length of $Fe_3O_4$ hollow chains in this work can reach the order of millimeters. Under such characteristic scales, the magnetic force among chains is much stronger than the random Brownian force. Thus, the translational and rotational Brownian motions are not considered. The gravity, buoyancy, moment of inertia, and inertia of chains are also neglected in the simulation.

**Governing Equations.** Considering all the aforementioned forces and torques, the equation of motion of each chain can be concluded as

$$\sum_{i=1}^{N}\left[\sum_{j=1,j\neq i}^{N_p}(\boldsymbol{F}_{ij}^m + \boldsymbol{F}_{ij}^{vdw} + \boldsymbol{F}_{ij}^r)\right] + \boldsymbol{F}^d = \boldsymbol{0} \tag{14}$$

$$\sum_{i=1}^{N}\left[(\boldsymbol{r}_i - \boldsymbol{r}_c) \times \sum_{j=1,j\neq i}^{N_p}(\boldsymbol{F}_{ij}^m + \boldsymbol{F}_{ij}^{vdw} + \boldsymbol{F}_{ij}^r)\right] + \boldsymbol{T}^m + \boldsymbol{T}^d = \boldsymbol{0} \tag{15}$$

where $N_p$ is the total number of hollow spheres. The kinematic equation of a single nanosphere is



DOI: 10.1021/acs.langmuir.9b01957
Langmuir 2019, 35, 12158−12167

$$\sum_{j=1,j\neq i}^{N_p} (\boldsymbol{F}_{ij}^{m} + \boldsymbol{F}_{ij}^{vdw} + \boldsymbol{F}_{ij}^{r} + \boldsymbol{F}_{ij}^{c}) + \boldsymbol{F}_{i}^{d} = \boldsymbol{0} \tag{16}$$

where $\boldsymbol{F}_{ij}^{c}$ is the constraint force acting between the adjacent hollow spheres in the same chain. Both $\boldsymbol{F}_{ij}^{r}$ and $\boldsymbol{F}_{ij}^{c}$ belong to the elastic force of $Fe_3O_4$. They are separated according to their different effects. $\boldsymbol{F}_{ij}^{r}$ is always along the radial direction and avoids the overlap among hollow spheres. $\boldsymbol{F}_{ij}^{c}$ possesses both radial and tangential component and drives the rotation of hollow spheres relative to the center of the chain. This constraint force has no effect on the motion of chains and only works in the calculation of shear stress. The magnetic potential energy $U_m$ and magnetoinduced stress $\sigma$ are written as

$$U_m = \mu_0 \left[ \sum_{i=1}^{N_p} - \boldsymbol{m}_i \cdot \boldsymbol{H} + \sum_{i=1}^{N_p-1} \sum_{j=i+1}^{N_p} \frac{1}{4\pi r_{ij}^{3}} (\boldsymbol{m}_i \cdot \boldsymbol{m}_j - 3\boldsymbol{m}_i \cdot \hat{\boldsymbol{r}} \, \boldsymbol{m}_j \cdot \hat{\boldsymbol{r}}) \right] \tag{17}$$

$$\sigma = \frac{1}{V} \left[ \sum_{i=1}^{N_p-1} \sum_{j=i+1}^{N_p} \boldsymbol{r}_{ij} (\boldsymbol{F}_{ij}^{m} + \boldsymbol{F}_{ij}^{vdw} + \boldsymbol{F}_{ij}^{r} + \boldsymbol{F}_{ij}^{c}) - \frac{1}{2} \sum_{chain} \varepsilon \cdot \boldsymbol{T}^{m} \right] \tag{18}$$

where $V$ is the volume of the simulation box and $\varepsilon$ is the alternating unit tensor. The last term in eq 18 is an antisymmetric component caused by the external field.[43]

## RESULTS AND DISCUSSION

**Experimental Results.** Typical microscopic images of $Fe_3O_4$ hollow chains are shown in Figure 1a–c. The SEM images show that these chains were composed of uniform nanospheres with nonuniform lengths ranging from 1 to 3 $\mu$m. The mean length and distribution of $Fe_3O_4$ hollow chains are evaluated to be $N$ = 6 and $N$ = 3–9 by measuring the dimensions of 30 chains from the SEM images. Obvious hollow features were revealed in the high-definition TEM image (inset of Figure 1c). The diameter and wall thickness of hollow nanospheres were estimated to be 300 and 60 nm, respectively. The magnetic hysteresis loop of $Fe_3O_4$ hollow chains is shown in Figure 1d. The samples possessed excellent super-paramagnetic characteristic in which the residual magnetism and coercive force were nearly zero. The saturation magnetization of $Fe_3O_4$ hollow chains was 90.9 emu/g, which was very close to that of bulk $Fe_3O_4$ (≈92 emu/g). Solid lines in Figure 1d are the fitting curves of the Langevin function, of which the coefficient of determination ($R^2$) is 0.9997. Constant $x$ in eq 1 was determined to be 244 $Oe^{-1}$.

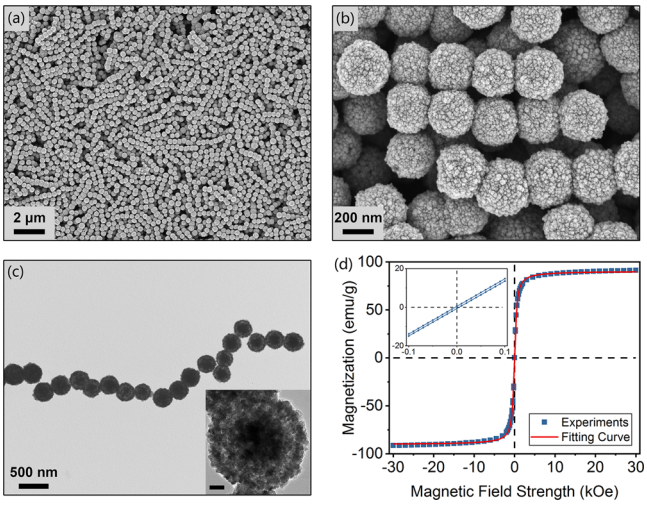


**Figure 1.** (a,b) SEM images of $Fe_3O_4$ hollow chains. (c) TEM images of $Fe_3O_4$ hollow chains. Inset: high-definition TEM graph, the scale bar is 50 nm. (d) Magnetic hysteresis loop and the fitting curves of $Fe_3O_4$ hollow chains. Inset: magnetic hysteresis loop between −100 and 100 Oe.

The rheological properties of magnetic fluids based on $Fe_3O_4$ hollow chains are presented in Figure 2. In the magnetic field sweep tests, the shear stress curves can be divided into two phases. Shear stress first increased with increasing external field. If the magnetic flux density exceeded a critical value, shear stress decreased for the 10 and 15 wt % magnetic fluids, which was different from pure hollow sphere magnetic fluid. The critical magnetic flux densities of the 10 and 15 wt % magnetic fluids were 120 and 168 mT, respectively. This trend was more obvious in dilute magnetic fluids, indicating that this phenomenon was caused by the rearrangement of $Fe_3O_4$ chains. For the 20 wt % magnetic fluid, the shear stress reached a plateau after the $Fe_3O_4$ hollow chains reached saturation magnetization. Figure 2b–d shows the flow curves of magnetic fluids with different weight fractions under different magnetic fields. In the absence of an external field, $Fe_3O_4$ hollow chains uniformly distributed in the matrix and gave no contribution to the shear stress. The samples exhibited Newtonian fluid characteristics in which the off-state viscosity under a high shear rate ($\eta_\infty$ = 0.005 Pa·s) was very close to the viscosity of water. After applying the magnetic field, $Fe_3O_4$ hollow chains interacted with each other and formed some particular microstructures. In order to make the sample flow, the shear loading should first overcome the initial microstructures. Magnetic fluids exhibited static yield stress $\tau_y$. If the shear stress was smaller than this value, the suspension showed

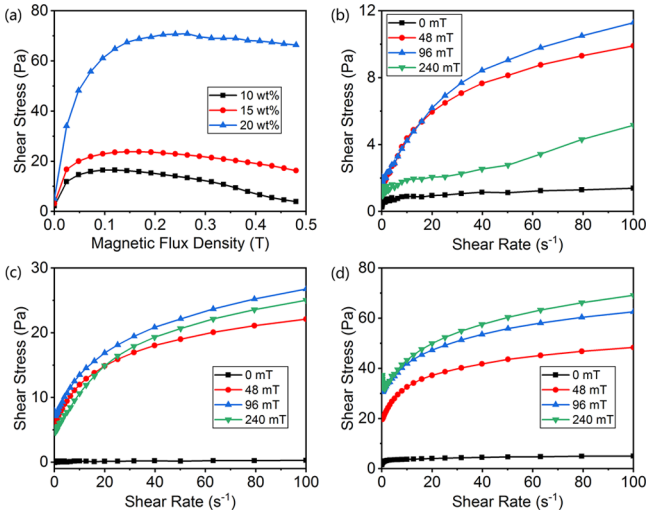


**Figure 2.** (a) Shear stress versus external magnetic field of magnetic fluid with different weight fractions. Flow curves of the magnetic fluid under different magnetic fields: (b) 10, (c) 15, and (d) 20 wt %.



DOI: 10.1021/acs.langmuir.9b01957
Langmuir 2019, 35, 12158–12167

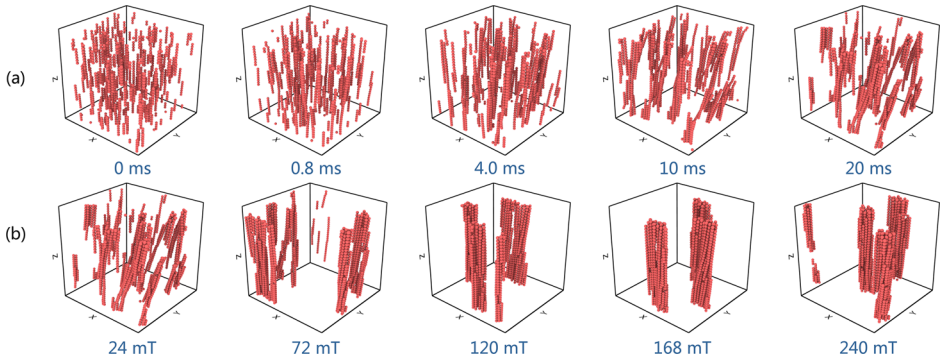


**Figure 3.** (a) Evolution of microstructures of 10 wt % magnetic fluid based on $Fe_3O_4$ hollow chains. (b) Microstructures at the end of the simulation under different magnetic fields.

a solid-like state. In the steady shear flow, microstructures would incline toward the shear direction and underwent continuous destruction and reformation processes. The average orientation of microstructures was influenced by the shear rate. Thus, the shear stress increased, while the viscosity declined with increasing shear rate, indicating shear thinning behaviors. Under a high shear rate, typical Bingham properties were observed. The flow curves can be described as

$$\tau = \tau_0 + \eta_p \dot{\gamma} \tag{19}$$

where $\tau_0$ is known as the dynamic yield stress, which is usually larger than $\tau_y$. $\eta_p$ stands for the post-yield viscosity. Both $\tau_0$ and $\eta_p$ increased with the external magnetic field and the concentration of $Fe_3O_4$ hollow chains. The dynamic yield stress of the 20 wt % magnetic fluid under 240 mT was 49.4 Pa. The post-yield viscosity reached 0.21 Pa·s, which was 2 orders of magnitude larger than $\eta_\infty$. Generally speaking, the shear stress should always increase with increasing magnetic field before saturation. However, under a small weight fraction and a strong external field, $Fe_3O_4$ hollow chains might agglomerate near the parallel plates. The destruction and reformation of microstructures also had a great influence on the shear stress. The flow curve at 240 mT was unusually lower than those under weaker magnetic fields. This phenomenon was consistent with the results in the magnetic field sweep. In Figure 2b, the local volume fraction of $Fe_3O_4$ was too small at 240 mT due to the agglomeration and formation of microstructures. Therefore, the shear stress at 240 mT is similar to that at 0 mT.

**Magnetoinduced Microstructures and Shear Stress in Magnetic Field Sweep.** In order to better comprehend the MR mechanism of $Fe_3O_4$ hollow chains, the magnetoinduced microstructures and shear stress were first analyzed. Evolution of the microstructures of 10 wt % magnetic fluid is plotted using the OVITO software (Figure 3a).[44] Here, the concentration of magnetic fluid was set at 10 wt %, while the shear rate was 100 $s^{-1}$. The sample was in a chaotic state at the start of simulations. $Fe_3O_4$ hollow chains were assumed to possess the same initial orientation in order to avoid the overlap among chains. After applying the magnetic field and shear flow, $Fe_3O_4$ chains rapidly aggregated along the field direction ($z$ axis) due to the principle of minimum energy. Chains arranged head-to-tail to form longer chain-like microstructures. Under a weak magnetic field (24 mT), chain-like microstructures then inclined toward the shear direction ($x$ axis). In such a configuration, each $Fe_3O_4$ hollow chain experienced a magnetic torque from the external field and could resist the hydrodynamic torque from the shear flow. At 10 ms after the start of the simulation, inclined chain-like microstructures further aggregated along the $x$ axis, forming cluster-like microstructures under a 24 mT magnetic field. Those clusters were disrupted by the shear flow and reconstructed under the magnetic dipolar forces. The disruption and reconstruction process could be displayed in the shear stress and magnetic potential energy curves. Finally, the magnetic fluid reached dynamic equilibrium. Microstructures of the 10 wt % magnetic fluid under different magnetic fields are shown in Figure 3b. The shear rate was maintained at 100 $s^{-1}$. Under a 24 mT magnetic field, inclined cluster-like microstructures were formed. With increasing magnetic flux density, the cluster-like aggregates rotated toward the field direction and merged into several larger columns. If the magnetic field strength exceeded 120 mT, microstructures showed familiar characteristics. Only a few large columns were observed in the simulation box. The dip angle was too small to be considered.

Under a weak magnetic field, the potential energy sharply decreased into a trough after the simulation started (Figure 4a). This phenomenon corresponded to the formation of the head-to-tail configuration of $Fe_3O_4$ hollow chains. Then the magnetoinduced shear stress monotonically increased versus time in 10 ms, which reflected the inclination of chain-like microstructures. After that, both magnetic potential energy and shear stress fluctuated around an average value. The destruction and reconstruction of cluster-like microstructures were confirmed. The average shear stress between 10 ms and the end of the simulation could represent the macroscopic mechanical properties in dynamic equilibrium. It is noteworthy that the peaks in the shear stress curve represented the disrupted state. Because the magnetic dipolar force (eq 5) is inversely proportional to the fourth power of distance, $Fe_3O_4$ hollow chains were more close to each other and generated stronger shear stress in the disrupted microstructures. However, this state was unstable due to the relatively high magnetic potential energy. $Fe_3O_4$ hollow chains would spontaneously form cluster-like microstructures again. Under a strong magnetic field (Figure 4b), the fluctuation range of shear stress became larger, while the fluctuation range of magnetic energy was smaller. The minimum value of shear stress corresponded to the fully formed column-like microstructures. There were only weak interactions among the columns; hence, the shear stress was weakened. The peaks in shear stress also reflected the disrupted microstructures. The



DOI: 10.1021/acs.langmuir.9b01957
Langmuir 2019, 35, 12158−12167

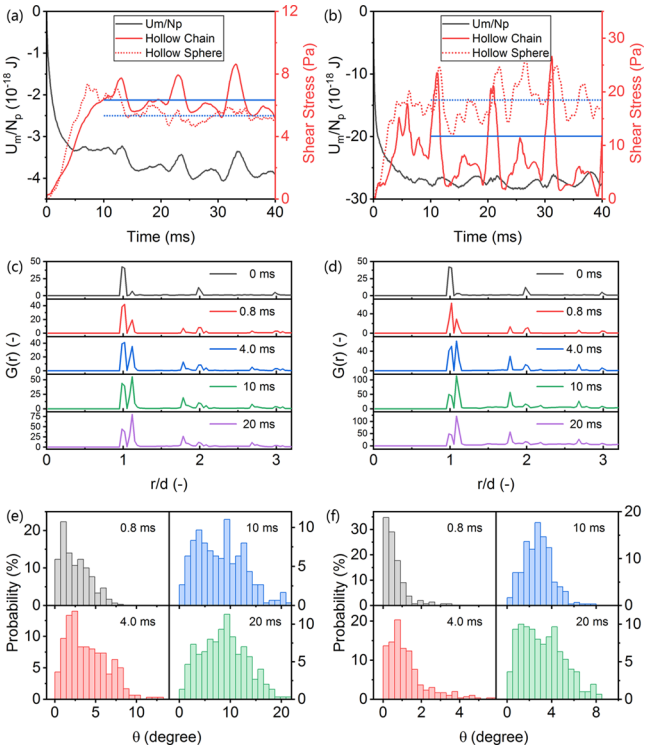


**Figure 4.** Magnetic potential energy of $Fe_3O_4$ hollow chains and shear stress of magnetic fluid based on $Fe_3O_4$ hollow chains and hollow spheres under magnetic fields of (a) 24 and (b) 240 mT. Vertical dashed lines represent $t$ = 0.8, 4.0, 10, and 20 ms. Radial distribution function at different times under magnetic fields of (c) 24 and (d) 240 mT. Histogram of the dip angles of $Fe_3O_4$ hollow chains at different times under magnetic fields of (e) 24 and (f) 240 mT.

maximum shear stress was 26.63 Pa, 2.27 times of the average shear stress (11.73 Pa).

The response speed is another key performance of magnetic fluid. In this work, the response time was defined as the time when shear stress reached 90% of the average shear stress. When the shear stress first decreased to the average shear stress, magnetic fluid was considered to reach dynamic equilibrium. The shear stress curves of 10 wt % magnetic fluid based on $Fe_3O_4$ hollow spheres were also plotted in Figure 4a,b to evaluate the response properties. Horizontal solid and dotted lines represent the average shear stress. The shear stress comparison is discussed in the following section. $Fe_3O_4$ hollow spheres presented shorter response and equilibrium time under a 24 mT magnetic field (Table 1). Because the magnetic interactions increased slower than the viscous forces with increasing chain length, hollow chains required more time to form particular microstructures. The response speed of both kinds of magnetic fluids increased together with the external field. Stronger magnetic interactions accelerated the evolution of microstructures. Under a 240 mT magnetic field, hollow chains possessed a shorter response time due to the decrease of average shear stress. Generally, the response times of both kinds of magnetic fluids were in the order of milliseconds. The chain morphology did not obviously weaken the response property of the magnetic fluid.

**Table 1. Response Time and Time To Reach Dynamic Equilibrium of Magnetic Fluid Based on $Fe_3O_4$ Hollow Chains and Hollow Spheres under Different Magnetic Fields**

| magnetic fluid | magnetic field | response time (ms) | equilibrium time (ms) |
|---|---|---|---|
| sphere | 24 mT | 4.80 | 13.68 |
| | 240 mT | 3.82 | 6.56 |
| chain | 24 mT | 7.70 | 14.16 |
| | 240 mT | 3.78 | 6.68 |

The aggregation of $Fe_3O_4$ hollow chains was quantified by the radial distribution function (RDF) and dip angle of chains. The RDF of $Fe_3O_4$ hollow spheres was obtained from the integration of pair distribution function[45]

$$g(r, \theta) = \frac{V}{N_p^2}\left\langle \sum_i \sum_{j\neq i} \delta(r - r_{ij})\delta(\theta - \theta_{ij}) \right\rangle \tag{20}$$

$$g(r) = \int_0^\pi g(r, \theta)\sin\theta \mathrm{d}\theta \tag{21}$$

where the bracket represents volume average. This parameter reflects the array of hollow spheres in a single chain and the compactness of microstructures. At the initial state, only the peaks at $r/d$ = 1, 2, 3, ..., were observed (Figure 4c). The rest of the curve was close to unity. The short-range $Fe_3O_4$ hollow chain and random distribution of chains were confirmed. As the simulation carried on, three peaks at $r/d$ = 1.08, 1.78, and 2.68 appeared, which originated from the aggregation of chains. When the cluster-like microstructures were formed, the newly generated peaks exceeded the initial peaks. The RDFs also fluctuated with the disruption and reconstruction of microstructures. The peak value reached its maximum when the magnetic potential energy reached the minimum. If the external magnetic field increased to 240 mT, the peak values at $r/d$ = 1.08, 1.78, and 2.68 obviously increased (Figure 4d). However, the initial peak values of RDF curves remained the same. Column-like microstructures were more compact than cluster-like microstructures. The dip angle of $Fe_3O_4$ hollow chains also had a great influence on the shear stress. If the angle between $\hat{\mathbf{r}}$ and the external field was 25°, the magnetic dipolar force showed the maximum contribution to the shear stress.[30] The histograms of the dip angle of $Fe_3O_4$ hollow chains are plotted in Figure 4e,f. Soon after the start of shear flow, $Fe_3O_4$ hollow chains tilted to an angle between 0 and 8°. Both the range of dip angle and the most probable dip angle increased with the development of shear flow. Finally, all the chains possessed an inclination between 0 and 22°. The most probable dip angle was 9−10° under a magnetic field of 24 mT. The range of dip angles decreased with increasing magnetic field. It is noted that the simulated magnetic moment vector of each chain was very close to the axis of the chain. According to eq 6, only a small dip angle can make the magnetic torque balanced with hydrodynamic torque under a strong external field. Finally, the dip angle became an approximately uniform distribution with a mean value of 3.2°.

The comparison between experimental and simulated shear stress in the magnetic field sweep is shown in Figure 5a, and the simulations matched well with experiments. Only a small difference was obtained when $B$ = 24 mT and $B \geq$ 144 mT. Simulations slightly underestimated the shear stress, which was due to the approximation of viscous torque. The decrease of shear stress when $B \geq$ 120 mT was also obtained in the simulation. Figure 5b shows the magnetic potential energy per hollow sphere ($U_m/N_p$) under different magnetic fields. Here, the average value from 10 ms to the end of the simulations



DOI: 10.1021/acs.langmuir.9b01957
Langmuir 2019, 35, 12158−12167

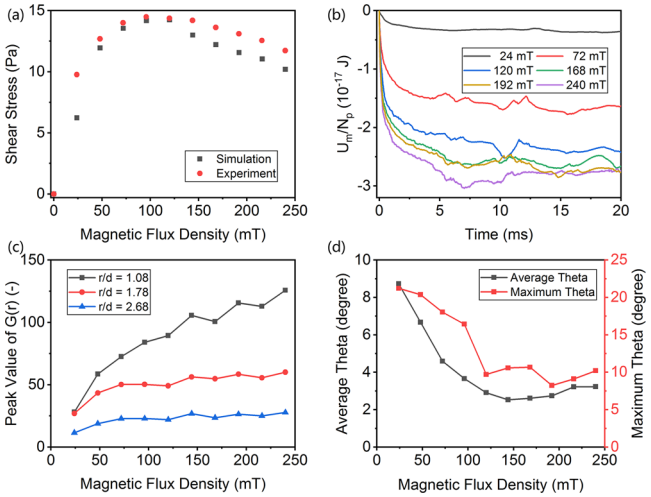


**Figure 5.** (a) Comparison between the experimental and simulated shear stress as a function of the external magnetic field. (b) Evolution of magnetic potential energy per hollow sphere under different magnetic fields. (c) Peak values at $r/d$ = 1.08, 1.78, and 2.68 from RDF curves versus external magnetic field. (d) Average dip angle and maximum dip angle of $Fe_3O_4$ hollow chains as a function of magnetic flux density.

reflected the intensity of dipolar forces among hollow nanospheres. The magnitude of magnetic potential energy sharply increased and then gradually increased with increasing magnetic field. Stronger magnetic dipolar forces would generate larger shear stress. The peak values at $r/d$ = 1.08, 1.78, and 2.68 from RDF curves as a function of magnetic flux density are plotted in Figure 5c. Here, the peak values were obtained from the RDF curves when instantaneous shear stress was equal to average stress. All the peak values increased with increasing magnetic field. More compact microstructures were formed under larger external fields. The more compact the $Fe_3O_4$ hollow chains aggregated, the stronger the shear stress was. The average and maximum dip angles of $Fe_3O_4$ hollow chains are shown in Figure 5d. The average dip angle $\overline{\theta}$ first decreased from 8.73 to 2.53° with increasing magnetic field and reached a stable value when $B \geq 120$ mT. The maximum dip angle dropped from 21.2 to 8.3° following the same trend. Under a high magnetic field, the orientation of $Fe_3O_4$ hollow chains seldom influenced the shear stress. Strong magnetic dipolar forces made column-like microstructures to rapidly reconstruct. Microstructures maintained their fully formed state most of the time, which corresponded to the trough of shear stress. For a concentrated magnetic fluid, the local volume fraction of $Fe_3O_4$ hollow chains remained high, no matter whether the microstructures were destroyed; therefore, the shear stress would not decrease. In summary, the increasing dipolar forces and compactness of microstructures were always instrumental in the generation of shear stress. The strong reconstruction processes led to the decline of shear stress versus magnetic field. The agglomeration of chains near the boundaries was another reason for the decrease in shear stress. This phenomenon was not reflected in the simulations due to the limitation of the simulation scale.

**Simulation Results in Shear Rate Sweep.** The correlation between microstructures and shear stress of magnetic fluid in shear rate sweep is investigated in this section. Here, the concentration of $Fe_3O_4$ and the external field were set at 10 wt % and 96 mT, respectively. When the shear rate changed, the total time steps of simulation changed in proportion to ensure that the shear strain at the end of simulations remained the same. Simulation results were also validated by experiments (Figure 6). A good correspondence

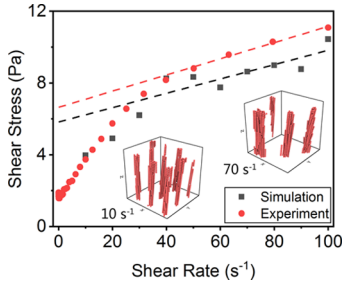


**Figure 6.** Comparison between the experimental and simulated shear stress as a function of shear rate. Dashed lines: fitting curves using the Bingham model. Inset: microstructures under shear rates of 10 and 70 $s^{-1}$.

between simulations and experiments was observed. Dashed lines represent the fitting curves of experimental and simulated shear stress using the Bingham model. The dynamic yield stresses of experiments and simulations were 6.6 and 5.8 Pa, while the post-yield viscosities were 0.045 and 0.040 Pa·s, respectively. Microstructures under two typical shear rates at the end of the simulation are plotted in the inset graphs. The results under various shear rates are shown in Figure S2. Under a shear rate of 10 $s^{-1}$, a large number of small column-like microstructures were observed in the simulation box. The number of columns decreased when the shear rate reached until 70 $s^{-1}$. The compactness of microstructures and intensity of dipolar forces remained the same in the shear rate sweep. The average dip angle of chains first increased until $\dot{\gamma}$ = 70 $s^{-1}$ and then decreased versus shear rate (Figure S3). Microstructures were easily destroyed into small pieces under a high shear rate. $Fe_3O_4$ hollow chains in this state also possessed strong shear stress. Generally, the growth of the dip angle was the main cause of the increasing shear stress when $\dot{\gamma} < 70$ $s^{-1}$, while the destruction of column-like microstructures became the main reason when $\dot{\gamma} \geq 70$ $s^{-1}$.

**Comparison between $Fe_3O_4$ Hollow Chains and Hollow Spheres.** In order to illustrate the merits and drawbacks of $Fe_3O_4$ hollow chains, the MR effects of magnetic fluids based on $Fe_3O_4$ hollow chains and $Fe_3O_4$ hollow spheres were compared. Here, the 10 wt % magnetic fluid was chosen as a sample. Monodisperse $Fe_3O_4$ hollow spheres and the hollow spheres in a chain possessed the same diameter and wall thickness. Figure 7a shows that $Fe_3O_4$ hollow chains exhibited a higher MR effect than hollow spheres when $B \leq$ 100 mT. The shear stress of hollow chains declined, while that of hollow spheres continued to increase until saturation magnetization. There was an excellent agreement between simulations and experiments. The comparison between 20 wt % magnetic fluids shows a familiar phenomenon (Figure S4). Simulation results under different weight fractions also matched well with experiments. In applications of magnetic fluid, the volume and energy consumption of the magnetic field device should be as small as possible. Magnetic fluids are supposed to exhibit a superior MR effect under a weak magnetic field. $Fe_3O_4$ hollow chains exactly satisfied this requirement. The magnetoinduced shear stress of hollow chains under a 48 mT magnetic field was 12.69 Pa, 52% larger



DOI: 10.1021/acs.langmuir.9b01957
Langmuir 2019, 35, 12158−12167

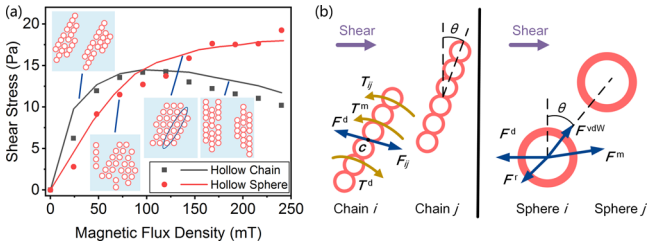


**Figure 7.** (a) Shear stress comparison between 10 wt % magnetic fluids based on $Fe_3O_4$ hollow chains and $Fe_3O_4$ hollow spheres. Lines: experiments; symbols: simulations. Inset: schematic diagram of microstructures under different magnetic fields. (b) Force analysis of magnetic fluid based on $Fe_3O_4$ hollow chains and $Fe_3O_4$ hollow spheres.

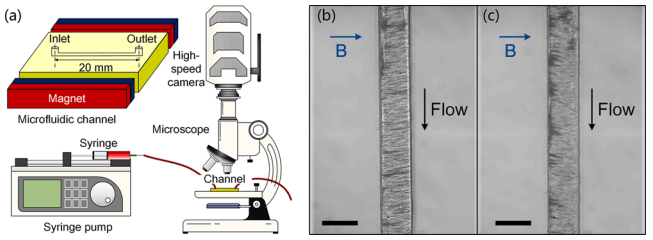


**Figure 8.** (a) Schematic diagram of the microfluidic channel and experimental setup. (b) Snapshots of the 10 wt % magnetic fluid in Poiseuille flow in a microfluidic channel. (c) Agglomeration of $Fe_3O_4$ hollow chains near the wall when increasing the magnetic field. Scale bar: 300 $\mu$m.

than that of hollow spheres. The difference between hollow chains and hollow spheres from the point of view of microstructures is illustrated in the inset graphs. Detailed microstructures are plotted in Figure S5.

The shear stress originated from the $x$ component of magnetic dipolar force and was influenced by the dip angle of microstructures. For a magnetic fluid based on $Fe_3O_4$ hollow chains, each chain experienced a resultant force from other chains, which was balanced with the hydrodynamic drag force (Figure 7b). The chains also experienced a magnetic torque from the external field, an interacting torque from other chains, and a viscous torque from the matrix. The dip angle of chains represented the inclination of microstructures, which was governd by the torque equilibrium. For a magnetic fluid based on hollow spheres, each sphere experienced a magnetic dipolar force, van der Waals force, repulsive force, and hydrodynamic drag force. The rotation of spheres did not influence the forces and is neglected in this section. The direction from sphere $i$ to sphere $j$ reflected the orientation of microstructures, which was governed by the force equilibrium. When increasing the external field, the magnetic dipolar forces of both kinds of magnetic fluids increased synchronously. For a hollow chain magnetic fluid, each chain possessed a large dip angle in order to generate a magnetic torque balanced with the viscous torque. The large $x$ component of dipolar force caused strong shear stress. For a hollow sphere magnetic fluid, each part of microstructures possessed different inclinations. The $x$ component of dipolar force among the hollow spheres is relatively small, leading to weak shear stress. Thus, the shear stress of $Fe_3O_4$ hollow chains grew faster than that of hollow spheres under a small magnetic field. If the external field further increased, the magnetic dipolar force further enhanced. The strong reformation process made $Fe_3O_4$ hollow chains vertically aligned most of the time. The $x$ component of the dipolar force and shear stress declined. However, for a hollow sphere magnetic fluid, the dip angle of microstructures hardly changed. Thus, the MR effect of hollow spheres exceeded that of hollow chains under a strong external field.

The experimental setup to observe the snapshots of magnetic fluid in Poiseuille flow is illustrated in Figure 8a. The microfluidic channel with a rectangular section of 270 $\mu$m × 100 $\mu$m was fabricated in a piece of polydimethylsiloxane using the standard soft-lithography technique.[46] A pair of permanent magnets generated a homogeneous 43 mT magnetic field perpendicular to the channel. The volume of flow was set at 0.3 mL/h and the frame rate of high-speed camera was 20000 fps. The weight fraction of magnetic fluid was 10 wt %. Figure 8b shows that $Fe_3O_4$ hollow chains formed large columns nearly parallel to the field. The columns often overtook each other due to the inhomogeneous velocity of the matrix in the channel. The evolution of microstructures in Poiseuille flow was also simulated using particle level dynamic simulations in which the same phenomenon was observed (Video S1). The simulation model of Poiseuille flow is discussed in Figure S6. This work belonged to the principal research on the hollow chain system. Thus, the concentration of $Fe_3O_4$ and magnetic flux density were relatively low. $Fe_3O_4$ hollow chains easily agglomerated near the wall of the channel under a strong magnetic field (Figure 8c) if the permanent magnets were closer to each other. The two main drawbacks of hollow chains, namely, agglomeration near the wall and decrease of shear stress versus magnetic field, can be overcome by improving the concentration of $Fe_3O_4$.

The Mason number is a useful tool to reveal the master curve of viscosity at various magnetic fields and shear rates. Klingenberg et al. define this dimensionless number as the ratio between hydrodynamic force and magnetic dipolar force $\mathrm{Mn} = F^{\mathrm{H}}/F^{\mathrm{M}}$.[47] For a system of $Fe_3O_4$ hollow chains, Mn can be expressed as[30]

$$\mathrm{Mn} = \frac{72\eta\xi_N\dot{\gamma}}{\mu_0 N M^2 S^2} \tag{22}$$

where $S$ = 84.8% is the solid proportion of $Fe_3O_4$ hollow spheres, $M$ is the magnetization of $Fe_3O_4$, and $\xi_N$ is determined using the average length of $Fe_3O_4$ hollow chains. Mn defined in this way involves the influence of matrix material, shear rate, external field, wall thickness of hollow spheres, and length of chains. Each parameter in eq 22 can be determined from experiments. Figure 9 shows that viscosity under each magnetic field was collapsed onto a linear master curve in a log−log coordinate. The slope of master curves was −1, indicating a typical Bingham characteristic. The complex

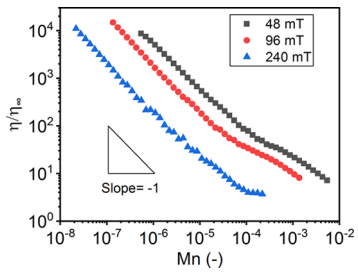


**Figure 9.** Dimensionless viscosity as a function of Mason number under different magnetic fields and shear rates.



DOI: 10.1021/acs.langmuir.9b01957
Langmuir 2019, 35, 12158−12167

evolution of microstructures governed the variation of shear stress and led to the separation of master curves.

## CONCLUSIONS

In this study, the MR mechanism of magnetic fluid based on $Fe_3O_4$ hollow chains was investigated using experiments and particle level dynamic simulations. $Fe_3O_4$ chains based on hollow spheres were synthesized and characterized. A special decrease of shear stress versus external field was obtained in dilute magnetic fluid when the magnetic flux density exceeded a critical value. However, the shear stress of concentrated magnetic fluid reached a plateau when the $Fe_3O_4$ hollow chains were magnetically saturated. All the magnetic fluids presented typical Bingham characteristics in the shear rate sweep.

Particle level dynamic simulations revealed that inclined cluster-like microstructures were formed under a weak field and vertical column-like microstructures were obtained under a strong field. The microstructures underwent a dynamic equilibrium between destruction and reconstruction. The shear stress fluctuated around the average value. The peaks in the shear stress curve corresponded to the disrupted state, while the troughs represented the fully formed state. In the magnetic field sweep, the compactness of microstructures and magnetic dipolar forces always increased with increasing magnetic flux density. For a dilute magnetic fluid, microstructures were in the fully formed state most of the time under a strong field, which led to the decrease of average shear stress. The agglomeration of chains near the boundaries was another reason for the decrease of shear stress. In the shear rate sweep, the increasing dip angle of chains enlarged the shear stress when $\dot{\gamma} \leq 70\ s^{-1}$. The destruction of microstructures further improved the shear stress if $\dot{\gamma} > 70\ s^{-1}$. The $Fe_3O_4$ hollow chains exhibited higher MR effect under a small external field when compared with conventional $Fe_3O_4$ hollow nanospheres. Chain morphology enlarged the dip angle of microstructures and thus generated stronger shear stress. This merit made hollow chains available for small-scale applications with low energy consumption.

The accuracy of the simulation was qualitatively validated by the mesoscopic graphs in Poiseuille flow in a microfluidic channel and quantitatively confirmed by the comparison with rheological tests. Simulation results matched well with experiments. Finally, the viscosity was collapsed onto linear master curves by using the Mason number.

## ASSOCIATED CONTENT

### Supporting Information

The Supporting Information is available free of charge on the ACS Publications website at DOI: 10.1021/acs.langmuir.9b01957.

The Supporting Information is available free of charge on the ACS Publications website and contains:

Reason to choose the initial conditions; microstructures of magnetic fluid under different shear rates; RDF, average dip angle of chains, and magnetic potential energy per hollow sphere as a function of shear rate; shear stress comparison between 20 wt % magnetic fluids based on $Fe_3O_4$ hollow chains and hollow spheres; microstructures of 20 wt % magnetic fluids based on $Fe_3O_4$ hollow chains and $Fe_3O_4$ hollow spheres (PDF)

simulation model of magnetic fluid based on $Fe_3O_4$ hollow chains in Poiseuille flow (MP4)

## AUTHOR INFORMATION


### Corresponding Authors

*E-mail: xuansh@ustc.edu.cn (S.X.).
*E-mail: gongxl@ustc.edu.cn (X.G.).

### ORCID

Shouhu Xuan: 0000-0002-8232-9736
Xinglong Gong: 0000-0001-6997-9526


### Author Contributions

The manuscript was written through the contributions of all authors. All authors have given approval to the final version of the manuscript.

### Notes

The authors declare no competing financial interest.

## ACKNOWLEDGMENTS

This work is supported by the National Natural Science Foundation of China (Grant Nos. 11822209, 11572309, and 11572310). The Collaborative Innovation Center of Suzhou Nano Science and Technology is gratefully acknowledged.

## REFERENCES


(1) De Vicente, J.; Klingenberg, D. J.; Hidalgo-Alvarez, R. Magnetorheological Fluids: a Review. *Soft Matter* **2011**, *7*, 3701−3710.

(2) Vékás, L. Ferrofluids and Magnetorheological Fluids. *Adv. Sci. Tech.* **2008**, *54*, 127−136.

(3) Li, W.; Zhang, X. The Effect of Friction on Magnetorheological Fluids. *Korea-Aust. Rheol. J.* **2008**, *20*, 45−50.

(4) Chae, H. D.; Choi, S.-B. A New Vibration Isolation Bed Stage with Magnetorheological Dampers for Ambulance Vehicles. *Smart Mater. Struct.* **2015**, *24*, No. 017001.

(5) Khan, D. A.; Jha, S. Selection of Optimum Polishing Fluid Composition for Ball End Magnetorheological Finishing (BEMRF) of Copper. *Int. J. Adv. Manuf. Technol.* **2019**, *100*, 1093−1103.

(6) Sun, S.; Yang, J.; Li, W.; Du, H.; Alici, G.; Yan, T.; Nakano, M. Development of an Isolator Working with Magnetorheological Elastomers and Fluids. *Mech. Syst. Signal Proc.* **2017**, *83*, 371−384.

(7) Potnuru, M. R.; Wang, X.; Mantripragada, S.; Gordaninejad, F. A Compressible Magneto-Rheological Fluid Damper-Liquid Spring System. *Int. J. Vehicle Des.* **2013**, *63*, 256−274.

(8) Xing, Z.; Yu, M.; Sun, S.; Fu, J.; Li, W. A Hybrid Magnetorheological Elastomer-Fluid (MRE-F) Isolation Mount: Development and Experimental Validation. *Smart Mater. Struct.* **2016**, *25*, No. 015026.

(9) Chiu-Lam, A.; Rinaldi, C. Nanoscale Thermal Phenomena in the Vicinity of Magnetic Nanoparticles in Alternating Magnetic Fields. *Adv. Funct. Mater.* **2016**, *26*, 3933−3941.

(10) Das, P.; Colombo, M.; Prosperi, D. Recent Advances in Magnetic Fluid Hyperthermia for Cancer Therapy. *Colloids Surf., B* **2019**, *174*, 42−55.

(11) Wang, J.; Fang, J.; Fang, P.; Li, X.; Wu, S.; Zhang, W.; Li, S. Preparation of Hollow Core/Shell $Fe_3O_4$@graphene Oxide Composites as Magnetic Targeting Drug Nanocarriers. *J. Biomater. Sci., Polym. Ed.* **2016**, *28*, 337−349.

(12) Anupama, A. V.; Kumaran, V.; Sahoo, B. Magnetorheological Fluids Containing Rod-Shaped Lithium-Zinc Ferrite Particles: the Steady-State Shear Response. *Soft Matter* **2018**, *14*, 5407−5419.

(13) López-López, M. T.; Kuzhir, P.; Bossis, G. Magnetorheology of Fiber Suspensions. I. Experimental. *J. Rheol.* **2009**, *53*, 115−126.

(14) Plachy, T.; Cvek, M.; Kozakova, Z.; Sedlacik, M.; Moucka, R. The Enhanced MR Performance of Dimorphic MR Suspensions Containing Either Magnetic Rods or Their Non-Magnetic Analogs. *Smart Mater. Struct.* **2017**, *26*, No. 025026.

(15) Zhang, K.; Piao, S. H.; Choi, H. J. Hollow Structured Magnetic Particles of $CoFe_2O_4$ and Their Magnetorheological Characteristics. *IEEE T. Magn.* **2015**, *51*, 1−4.




DOI: 10.1021/acs.langmuir.9b01957
*Langmuir* 2019, 35, 12158−12167

(16) Fang, F. F.; Kim, J. H.; Choi, H. J. Magnetorheological Characterization of Hollow Polymer/Magnetite Microspherical Composite. *Int. J. Mod. Phys. B* **2012**, *23*, 3613−3618.
(17) Cong, Y.; Wang, G.; Xiong, M.; Huang, Y.; Hong, Z.; Wang, D.; Li, J.; Li, L. A Facile Interfacial Reaction Route to Prepare Magnetic Hollow Spheres with Tunable Shell Thickness. *Langmuir* **2008**, *24*, 6624−6629.
(18) Chang, Y.; Li, Y.; Song, J.; Zhao, M.; Guo, J.; An, Q.; Gong, Y.; Guo, Q. Formaldehyde Controlling the Synthesis of Multishelled SiO2/FexOyHollow Porous Spheres. *Langmuir* **2018**, *34*, 8223−8229.
(19) Cheng, W.; Tang, K.; Qi, Y.; Sheng, J.; Liu, Z. One-Step Synthesis of Superparamagnetic Monodisperse Porous $Fe_3O_4$ Hollow and Core-Shell Spheres. *J. Mater. Chem.* **2010**, *20*, 1799−1805.
(20) Saha, P.; Mukherjee, S.; Mandal, K. Rheological Response of Magnetic Fluid Containing $Fe_3O_4$ Nano Structures. *J. Magn. Magn. Mater.* **2019**, *484*, 324−328.
(21) Ghaffari, A.; Hashemabadi, S. H.; Ashtiani, M. A Review on the Simulation and Modeling of Magnetorheological Fluids. *J. Intell. Mater. Syst. Struct.* **2014**, *26*, 881−904.
(22) Gharibvand, A. J.; Norouzi, M.; Shahmardan, M. M. Dissipative Particle Dynamics Simulation of Magnetorheological Fluids in Shear Flow. *J. Braz. Soc. Mech. Sci. Eng.* **2019**, *41*, 103.
(23) Morillas, J. R.; de Vicente, J. Yielding Behavior of Model Magnetorheological Fluids. *Soft Matter* **2019**, *15*, 3330−3342.
(24) Zhang, S.; Zhou, J.; Shao, C. Numerical Investigation on Yielding Phenomena of Magnetorheological Fluid Flowing through Microchannel Governed by Transverse Magnetic Field. *Phys. Fluids* **2019**, *31*, No. 022005.
(25) Bahiuddin, I.; Mazlan, S. A.; Shapiai, I.; Imaduddin, F.; Ubaidillah; Choi, S. B. Constitutive Models of Magnetorheological Fluids Having Temperature-Dependent Prediction Parameter. *Smart Mater. Struct.* **2018**, *27*, No. 095001.
(26) Klingenberg, D. J.; Vanswol, F.; Zukoski, C. F. Dynamic Simulation of Electrorheological Suspensions. *J. Chem. Phys.* **1989**, *91*, 7888−7895.
(27) Ruiz-López, J. A.; Fernández-Toledano, J. C.; Klingenberg, D. J.; Hidalgo-Alvarez, R.; de Vicente, J. Model Magnetorheology: a Direct Comparative Study between Theories, Particle-Level Simulations and Experiments, in Steady and Dynamic Oscillatory Shear. *J. Rheol.* **2016**, *60*, 61−74.
(28) Ruiz-López, J. A.; Wang, Z. W.; Hidalgo-Alvarez, R.; de Vicente, J. Simulations of Model Magnetorheological Fluids in Squeeze Flow Mode. *J. Rheol.* **2017**, *61*, 871−881.
(29) Ruan, X.; Pei, L.; Xuan, S.; Yan, Q.; Gong, X. The Rheological Responds of the Superparamagnetic Fluid Based on $_{Fe\,3\,O\,4}$ Hollow Nanospheres. *J. Magn. Magn. Mater.* **2017**, *429*, 1−10.
(30) Pei, L.; Pang, H.; Chen, K.; Xuan, S.; Gong, X. Simulation of the Optimal Diameter and Wall Thickness of Hollow Fe3O4 microspheres in Magnetorheological Fluids. *Soft Matter* **2018**, *14*, 5080−5091.
(31) Zubarev, A. Y.; Abu-Bakr, A. F.; Bossis, G.; Bulycheva, S. V. Hyperthermia in a System of Rod-Like Ferromagnetic Particles under Oscillating Magnetic Field. *Magnetohydrodynamics* **2014**, *50*, 397−406.
(32) Zubarev, A.; Chirikov, D. To the Theory of Rheological Properties of Magnetic Fluid Suspensions with Rod-Like Particles. *Magnetohydrodynamics* **2014**, *50*, 381−388.
(33) Satoh, A. Influence of the Spin Brownian Motion on the Negative Magneto-Rheological Effect in a Rod-Like Haematite Particle Suspension. *Mol. Phys.* **2013**, *111*, 1042−1052.
(34) Kim, K. H.; Kim, M.-J.; Choa, Y.-H.; Kim, D. H.; Yu, J.-H. Synthesis and Magnetic Properties of Surface Coated Magnetite Superparamagentic Nanoparticles. *IEEE T. Magn.* **2008**, *44*, 2940−2943.
(35) Liu, T.; Gong, X.; Xu, Y.; Xuan, S.; Jiang, W. Simulation of Magneto-Induced Rearrangeable Microstructures of Magnetorheological Plastomers. *Soft Matter* **2013**, *9*, 10069−10080.
(36) Faure, B.; Salazar-Alvarez, G.; Bergström, L. Hamaker Constants of Iron Oxide Nanoparticles. *Langmuir* **2011**, *27*, 8659−8664.
(37) Klingenberg, D. J.; Olk, C. H.; Golden, M. A.; Ulicny, J. C. Effects of Nonmagnetic Interparticle Forces on Magnetorheological Fluids. *J. Phys.: Condens. Matter* **2010**, *22*, 324101.
(38) de Vicente, J.; Ramírez, J. Effect of Friction between Particles in the Dynamic Response of Model Magnetic Structures. *J. Colloid Interface Sci.* **2007**, *316*, 867−876.
(39) Swanson, E.; Teller, D. C.; de Haën, C. The Low Reynolds Number Translational Friction of Ellipsoids, Cylinders, Dumbbells, and Hollow Spherical Caps. Numerical Testing of the Validity of the Modified Oseen Tensor in Computing the Friction of Objects Modeled as Beads on a Shell. *J. Chem. Phys.* **1978**, *68*, 5097−5102.
(40) Yang, K.; Lu, C.; Zhao, X.; Kawamura, R. From Bead to Rod: Comparison of Theories by Measuring Translational Drag Coefficients of Micron-Sized Magnetic Bead-Chains in Stokes Flow. *PLoS One* **2017**, *12*, No. e0188015.
(41) Yamakawa, H.; Tanaka, G. Translational Diffusion Coefficients of Rodlike Polymers: Application of the Modified Oseen Tensor. *J. Chem. Phys.* **1972**, *57*, 1537−1542.
(42) Roy, T.; Sinha, A.; Chakraborty, S.; Ganguly, R.; Puri, I. K. Magnetic Microsphere-Based Mixers for Microdroplets. *Phys. Fluids* **2009**, *21*, No. 027101.
(43) Sánchez, J. H.; Rinaldi, C. Magnetoviscosity of Dilute Suspensions of Magnetic Ellipsoids Obtained through Rotational Brownian Dynamics Simulations. *J. Colloid Interface Sci.* **2009**, *331*, 500−506.
(44) Stukowski, A. Visualization and Analysis of Atomistic Simulation Data with OVITO-the Open Visualization Tool. *Modelling Simul. Mater. Sci. Eng.* **2009**, *18*, No. 015012.
(45) Ruiz-López, J. A.; Wang, Z. W.; Fernández-Toledano, J. C.; Hidalgo-Alvarez, R.; de Vicente, J. Start-up Rheometry of Highly Polydisperse Magnetorheological Fluids: Experiments and Simulations. *Rheol. Acta* **2016**, *55*, 245−256.
(46) Wu, J.; Yan, Q.; Xuan, S.; Gong, X. Size-Selective Separation of Magnetic Nanospheres in a Microfluidic Channel. *Microfluid. Nanofluid.* **2017**, *21*, 47.
(47) Klingenberg, D. J.; Ulicny, J. C.; Golden, M. A. Mason Numbers for Magnetorheology. *J. Rheol.* **2007**, *51*, 883−893.



DOI: 10.1021/acs.langmuir.9b01957
*Langmuir* 2019, 35, 12158−12167